

Ionization potentials of transparent conductive indium tin oxide films covered with a single layer of fluorine-doped tin oxide nanoparticles grown by spray pyrolysis deposition

Tatsuo Fukano^{a)}

Toyota Central Research and Development Laboratories Inc., Nagakute, Aichi 480-1192, Japan
and Graduate School of Materials Science, Nara Institute of Science and Technology, Ikoma,
Nara 630-0192, Japan

Tomoyoshi Motohiro

Toyota Central Research and Development Laboratories Inc., Nagakute, Aichi 480-1192, Japan

Takashi Ida

Ceramics Research Laboratory, Nagoya Institute of Technology, Tajimi, Gifu 507-0071, Japan

Hiroo Hashizume

Research and Education Center for Materials Science, Nara Institute of Science and Technology, Ikoma,
Nara 630-0192, Japan

(Received 6 October 2004; accepted 11 January 2005; published online 8 April 2005)

Indium tin oxide (ITO) films deposited with single layers of monodispersive fluorine-doped tin oxide (FTO) nanoparticles of several nanometers in size were grown on glass substrates by intermittent spray pyrolysis deposition using conventional atomizers. These films have significantly higher ionization potentials than the bare ITO and FTO films grown using the same technique. The ITO films covered with FTO particles of 7 nm in average size show an ionization potential of 5.01 eV, as compared with ~ 4.76 and ~ 4.64 eV in ITO and FTO films, respectively, which decreases as the FTO particle size increases. The ionization potentials are practically invariant against oxidation and reduction treatments, promising a wide application of the films to transparent conducting oxide electrodes in organic electroluminescent devices and light-emitting devices of high efficiencies. © 2005 American Institute of Physics. [DOI: 10.1063/1.1866488]

I. INTRODUCTION

Transparent conducting oxide (TCO) electrodes are key elements in optoelectronic devices. In particular, indium tin oxide (ITO) films are widely used as TCO electrodes because of high optical transmittance and low electrical resistivity. Several attempts have been made to improve ITO electrodes by depositing other thin films on top of ITO films.^{1–3} ITO films covered with fluorine-doped tin oxide (FTO) films and antimony-doped tin oxide films were investigated to improve the stability against thermal oxidizing treatment¹ and to lower the electrical resistivity,^{2,3} respectively.

Meanwhile, it has emerged that the ionization potential of TCO electrodes plays an essential role in the efficiencies of organic electroluminescent devices and light-emitting devices.^{4–6} Several dry processes^{3,7,8} and wet processes^{5,6,9} have been investigated to control the ionization potentials of ITO films, which are promising materials for TCO electrodes. Attempts have been made as well to control the ionization potential by depositing other thin films on top of substrates.^{10–13} The surface photovoltage (SPV) of In_2O_3 overlayers on InP substrates shows an intriguing overlayer-thickness dependence, which is divided in three regions.¹¹ In the first region, the SPV sharply increases with overlayer thickness below ~ 2 nm and the increase rate is reduced in the second region located above ~ 2 nm. The third region is

featured by a decreasing SPV with overlayer thickness above ~ 10 nm. By contrast, the work function of an In_2O_3 overlayer on an InSe substrate monotonically decreases with overlayer thickness above ~ 0.8 nm.¹³ These observations show that the ionization potential of the In_2O_3 -deposited films varies with overlayer thickness below ~ 30 nm.

In the present work, we grow ITO films covered with single layers of monodispersive nanoparticles of FTO and investigate the ionization potential of the films for TCO electrodes along with various electrical, optical, and structural properties. We will show that the FTO/ITO bilayers have higher ionization potential than ITO or FTO films and that they are stable against oxidizing or reducing treatments.

II. EXPERIMENT

The ITO films covered with FTO nanoparticles were grown by intermittent spray pyrolysis deposition (SPD) using solutions of raw materials.¹⁴ The ITO films of high optical transmittance and low electrical resistivity were grown as well by intermittent SPD at relatively low temperatures of 300–350 °C.^{14–16} We prepared the solution for ITO films by dissolving 0.095 mol of $\text{InCl}_3 \cdot 2.7\text{H}_2\text{O}$ and 0.005 mol of $\text{SnCl}_2 \cdot 0.86\text{H}_2\text{O}$ in 1 l of $\text{C}_2\text{H}_5\text{OH}$, which was stirred for 2 h. The solution for FTO nanoparticles and films was prepared by dissolving 50 mmol of NH_4F in 50 ml of 2-M HCl. The mixture was diluted by 1 l of $\text{C}_2\text{H}_5\text{OH}$, into which we

^{a)}Electronic mail: e0987@mosk.tytlabs.co.jp

dissolved 0.1 mol of $\text{SnCl}_2 \cdot 0.86\text{H}_2\text{O}$. The solution was ultrasonically agitated for 10 min and stirred for 2 h.

We used perfume atomizers to manually spray the solutions on Corning 7059 glass substrates, $20 \times 30 \times 0.5$ mm,³ in size, in the atmosphere,¹⁴ which had been cleaned ultrasonically in organic solvents. The glass substrates were heated on a hot stage to ~ 340 °C. A thermocouple attached on the upper surface of a substrate monitored the temperature. The procedure we used to prepare ITO films covered with FTO nanoparticles is as follows. Firstly, thick ITO films are grown, and then FTO nanoparticles of various sizes are grown on top of them by varying the spray cycle number. We repeated 175 spray cycles for ITO films and 2, 5, and 10 spray cycles for FTO particles. A bare ITO film without FTO was grown by 175 spray cycles for reference. Three pseudo-films and a thick film of FTO were grown on glass substrates by 2, 5, 10, and 175 spray cycles to investigate the growth of FTO nanoparticles. Only a small amount of the solution (approximately 0.17 ml) was consumed in each cycle. The nozzle-to-substrate distance was ~ 20 cm. Laser diffraction revealed the droplet sizes of $43\text{--}97$ μm , with a mean value around 62 μm , at $15\text{--}25$ cm from the atomizer nozzle. During a spray shot, the substrate temperature was decreased to $325\text{--}330$ °C. The spraying operation was temporarily interrupted and resumed after the temperature returned to 340 °C. The average time interval between the sprays was ~ 5 s.

The nanostructures of the films were studied using a field-emission scanning electron microscope (FE-SEM; model JSM-890, JEOL). The average grain sizes of the nanoparticles were determined by the Heyn linear intercept procedure¹⁷ using the FE-SEM images. The optical transmittance spectra of the films were evaluated in the $400\text{--}800$ -nm wavelength range using an UV-VIS-NIR double-beam spectrophotometer (model 330, HITACHI). We placed no blank glass substrate in the reference beam path. The thicknesses of the films were calculated from interference fringes observed in the transmittance spectra. We estimated the band gaps of the films from the optical-absorption data. The surface compositions of the films were determined by x-ray photoelectron spectroscopy (XPS; model PHI-5500MC, ULVAC-PHI) using a probing x-ray beam of 800 μm in diameter. The crystalline properties of the films were studied by x-ray diffractometry using Cu K α radiation and synchrotron x rays at beamline BL-4B₂ of the Photon Factory, Tsukuba. The electrical properties, carrier density, Hall mobility, and sheet resistance of the films were measured at room temperature using the Van der Pauw method (model ResiTest 8300, TOYO). The probe current was 0.1 mA. The electric resistivity was calculated from the thickness and the sheet resistance.

We determined the ionization potentials of the films in the atmosphere using a low-energy photoelectron spectrometer with a side-window double-cylindrical-grid open counter (model AC-2, RIKEN KEIKI). A 4×4 mm³ area on the sample surface was illuminated by the probing ultraviolet beam, which covered an excitation energy range of $4.20\text{--}6.20$ eV. The oxidation treatment was carried out by heating the films to 450 °C and keeping them for 60 min in

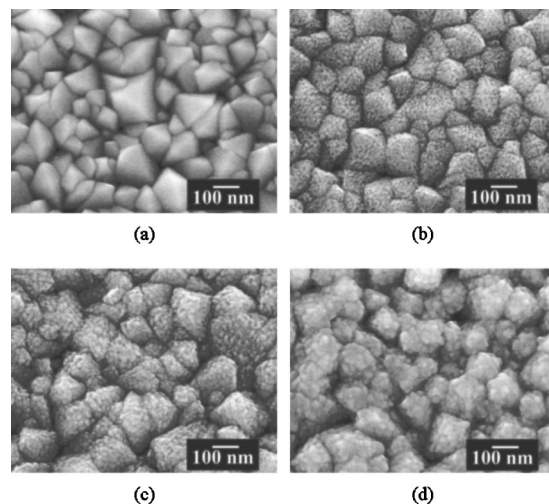


FIG. 1. Scanning electron microscope (SEM) images of the surface morphologies of (a) the ITO film and (b)–(d) three ITO films covered with FTO nanoparticles. (a) $N_F=0$, (b) $N_F=2$, (c) $N_F=5$, and (d) $N_F=10$, where N_F indicates the spray cycle number of the FTO solution.

the atmosphere. The reduction treatment was carried out by heating the films to 600 °C and keeping them for 60 min in 0.2 vol % H_2 balanced with N_2 .

III. RESULTS

Figure 1 shows the FE-SEM images of the surface structures of the ITO film and the three ITO films covered with FTO nanoparticles. The ITO film is regularly textured with grains of $50\text{--}150$ nm in size [Fig. 1(a)]. The ITO films covered with FTO nanoparticles are featured by seemingly monodispersive FTO particles of nanometer size, deposited on the large ITO crystallites [Figs. 1(b)–1(d)]. The size of the FTO nanoparticles increases with increasing the spray cycle number of FTO solution (N_F) from 2 to 10. Surprisingly, the FTO nanoparticles, regarded as spheres or roundish cubes, do not pile up on each other but form a single layer on the ITO grains, as evidenced in the FE-SEM images of the cross-sectional views (Fig. 2). The FTO nanoparticle size approxi-

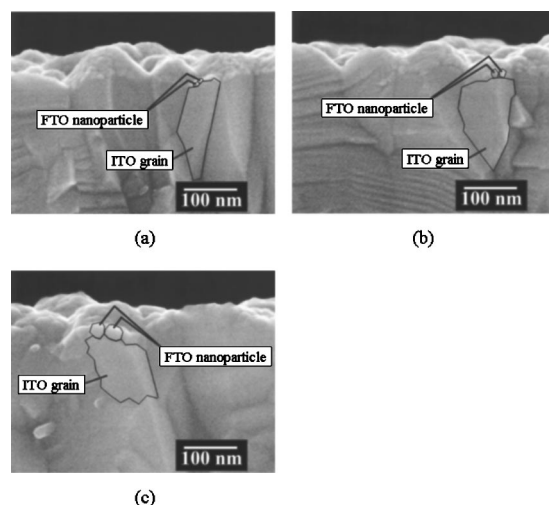


FIG. 2. SEM images of the cross sections of the three films covered with FTO nanoparticles. (a) $N_F=2$, (b) $N_F=5$, and (c) $N_F=10$. FTO nanoparticles form monolayers on ITO grains.

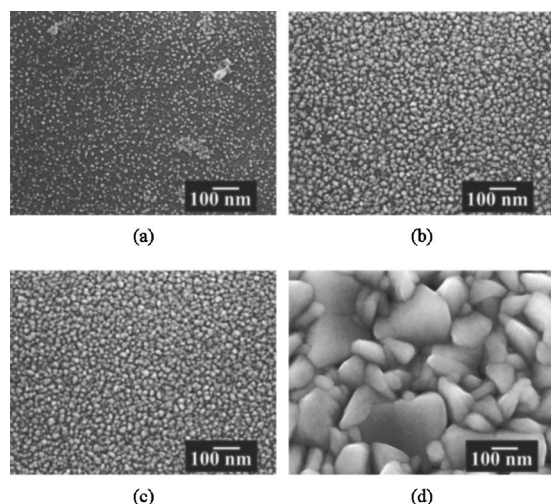


FIG. 3. SEM images of the surface morphologies of (a)–(c) three FTO pseudofilms and (d) a thick FTO film grown on glass substrates. (a) $N_F=2$, (b) $N_F=5$, and (c) $N_F=10$.

mately equals the thickness of the single layer of the FTO nanoparticles, which is estimated to be 7, 13, and 26 nm in Figs. 1(b)–1(d), respectively.

Figure 3 shows the FE-SEM images of the surface structures of three FTO pseudofilms and a thick FTO film grown on glass substrates. A surface morphology of the thick FTO film is quite similar to that of the thick ITO film [Fig. 1(a)]. We see in Fig. 3(d) bimodal grain sizes of 50–100 and 200–400 nm. The FTO pseudofilms are featured by apparently monodisperse particles of nanometer size [Figs. 3(a)–3(c)]. This is similar to the FTO particles deposited on the ITO substrate (Fig. 1). Increasing N_F from 2 to 10 results in gradually increasing grains. It is likely that FTO crystallites nucleate at all possible sites during initial spray cycles and that further sprayings contribute to the grain growth on both glass substrates and ITO substrates.

Figure 4 shows the optical transmittance spectra of the films. The mean transmittance is very high, $\sim 85\%$, in the 400–800-nm wavelength range. The optical absorptions of the ITO film and the glass substrate are negligible in this wavelength. This allows us to estimate the film thicknesses from the transmittances and the wavelengths at the minimal interference transmittance positions (see Appendix). The

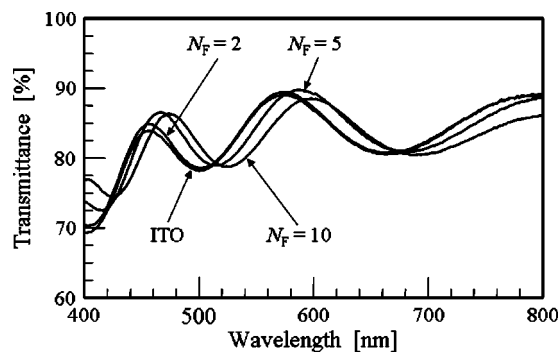


FIG. 4. Optical transmittance spectra of the ITO film and three ITO films covered with FTO nanoparticles ($N_F=2$, 5, and 10).

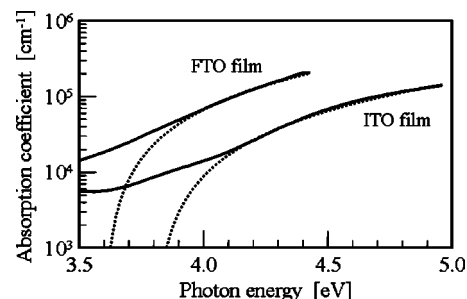


FIG. 5. Optical-absorption spectra of the ITO film and the FTO film. The broken lines show the fits obtained by applying $\alpha(\hbar\omega)=A_0(\hbar\omega-E_g)^{3/2}$ to the high-energy part of the spectra to estimate the optical band-gap energies.

thickness of the ITO film is thus estimated to be 450 nm, which agrees well with the value derived from the FE-SEM image.

Figure 5 shows the optical-absorption spectra of the ITO film and the FTO film. To determine the band-gap energy E_g , we fitted the high-energy part, $a(\hbar\omega)$, of the absorption spectra to

$$a(\hbar\omega)=A_0(\hbar\omega-E_g)^{3/2}, \quad (1)$$

where $\hbar\omega$ and A_0 are the photon energy and proportionality constant, respectively. Equation (1) applies to the direct-forbidden transition.^{18–21} The fits give $E_g \approx 3.8$ eV for the FTO film and 3.6 eV for the ITO film. The poor fits near the band-gap energies are due to the exciton excitation which is not included in Eq. (1).

Table I shows the chemical compositions of the surface layers of the films. We confirmed the presence of In, Sn, F, Cl, O, and C by XPS. The Sn/(In+Sn) atomic ratio on the ITO film surface is approximately 0.066, and the F/Sn atomic ratio on the FTO film surface is approximately 0.0074. The Sn/(In+Sn) ratio is not far from 5 at. % in the solution, whereas the F/Sn ratio is very much lower than the value in the solution (0.5). This shows that F easily evaporates away in the pyrolysis deposition procedure. In the FTO-nanoparticle-covered ITO films, the coverage is not complete because we detected In on their surfaces, which is not involved in FTO. If the coverage is complete, the In signal would not be observed since the detection depth of XPS is no greater than 3 nm. The exposed area of the ITO surface decreases with increasing size of FTO nanoparticles with N_F . Figures 1(b)–1(d) show that the FTO nanoparticles are iso-

TABLE I. Compositions of the surface layers of the ITO films covered with FTO nanoparticles, the ITO film, and the FTO film determined by XPS.

Average size of FTO nanoparticles	Atomic concentration [at. %]					
	In	Sn	F	Cl	O	C
(ITO film)	24.71	1.76	...	1.76	33.36	38.41
7 nm	7.36	18.96	0.81	0.32	40.39	32.79
13 nm	0.51	23.90	0.10	0.07	42.98	32.44
26 nm	0.30	27.38	0.13	0.10	47.62	24.47
(FTO film)	...	27.12	0.20	0.09	47.38	25.21

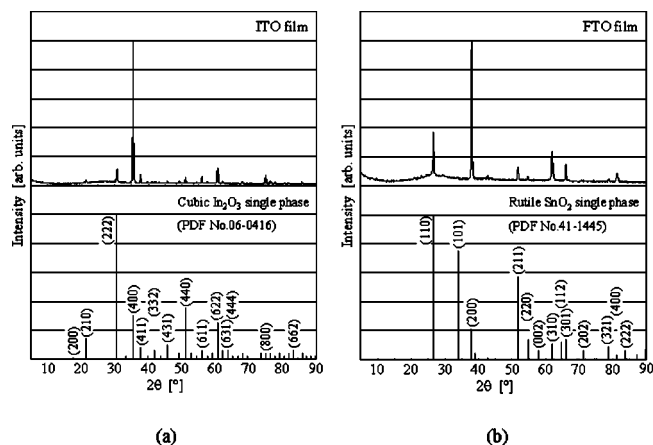


FIG. 6. X-ray powder patterns of (a) the ITO film and (b) the FTO film. Standard powder peak intensities obtained from the PDF files are shown in the bottom panels by vertical bars for (a) single-phase cubic In_2O_3 and (b) rutile-phase SnO_2 . Note the (400) and (200) preferred orientations in the ITO film and the FTO film, respectively.

lated from one another on the ITO grains, especially for 7- and 13-nm FTO nanoparticles. This is also the case on the glass substrate (Fig. 3).

We show in Fig. 6 the x-ray powder patterns of the ITO film and the FTO film. The observed reflection lines can be nicely indexed on the cubic lattices of In_2O_3 (Ref. 22) and the rutile phase of SnO_2 .²³ The significant deviations of the peak intensities from the standard powder pattern show significant preferred orientations in our films. The ITO film and the FTO film have the (400) and (200) preferred orientations, respectively. Figure 7 shows the x-ray patterns of three ITO films covered with FTO nanoparticles, along with the ITO film for reference. All reflection lines are attributed to cubic In_2O_3 except for one peak marked with an arrow. The arrowed peak, located at $2\theta=34^\circ$, grows as the average size of the FTO nanoparticles increases, which is identified as the (101) reflection of the rutile phase of SnO_2 .

We show in Fig. 8 a high-resolution x-ray powder pattern of the ITO film covered with FTO nanoparticles of 26 nm in average size, recorded at a synchrotron source. This pattern is obtained by deconvoluting the observed powder pattern with the instrumental function. The improved resolution is evident when one compares the In_2O_3 (200) and (210) peaks with those in Fig. 7. We note small unresolved peaks located at the (200), (111), and (211) positions of the rutile phase of SnO_2 , in addition to the obvious (101) peak. An attempt to separate the FTO peaks from the ITO peaks for further structure analyses was unsuccessful because of the too weak intensities of the FTO peaks. Nevertheless, it is highly likely that the FTO nanoparticle has the crystal structure of the rutile phase of SnO_2 . It is also inferred that the crystal structure of the FTO nanoparticles does not show a steep change with decreasing the average size of the FTO nanoparticles from 26 to 7 nm (Fig. 7).

The Hall mobility and the carrier density of the 400-nm-thick ITO film are approximately $37 \text{ cm}^2 \text{ V}^{-1} \text{ s}^{-1}$ and $4.7 \times 10^{20} \text{ cm}^{-3}$, respectively. On the other hand, the Hall mobility and the carrier density of the 400-nm-thick FTO film are approximately $28 \text{ cm}^2 \text{ V}^{-1} \text{ s}^{-1}$ and $3.0 \times 10^{20} \text{ cm}^{-3}$.

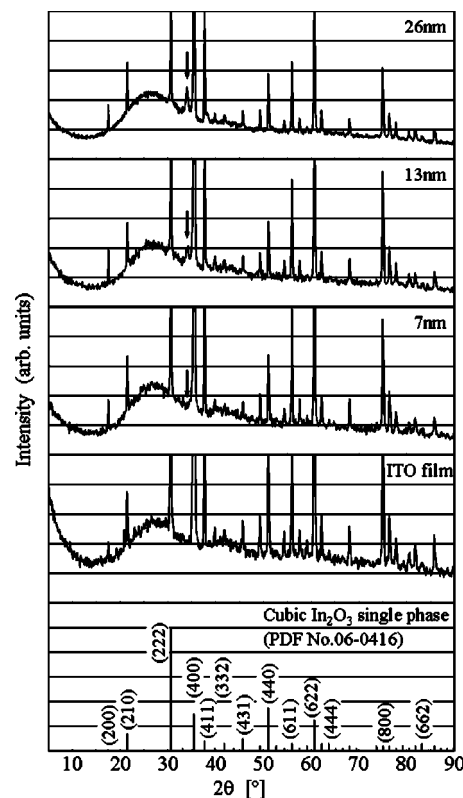


FIG. 7. X-ray powder patterns of the ITO film and three ITO films covered with FTO nanoparticles of 7, 13, and 26 nm in average size. The diffraction peaks marked with arrows are attributed to rutile-phase SnO_2 . All other peaks are indexed on the cubic In_2O_3 lattice.

Note that the carrier density is very high, greater than 10^{20} cm^{-3} in both ITO and FTO films. The film resistivities of the ITO film and the FTO film are 3.5×10^{-4} and $7.4 \times 10^{-4} \Omega \text{ cm}$, respectively.

Figure 9 shows the ionization potentials of the ITO films covered with FTO nanoparticles as a function of the average size of the FTO nanoparticles. The ITO film and the FTO film have the ionization potentials of ~ 4.76 and ~ 4.64 eV, respectively. These are approximately in agreement with the reported values.^{24–26} A salient feature of the ionization potential of the ITO film covered with FTO nanoparticles is that it is significantly higher than those for the ITO film and the FTO film. The ITO surface deposited with FTO nanopar-

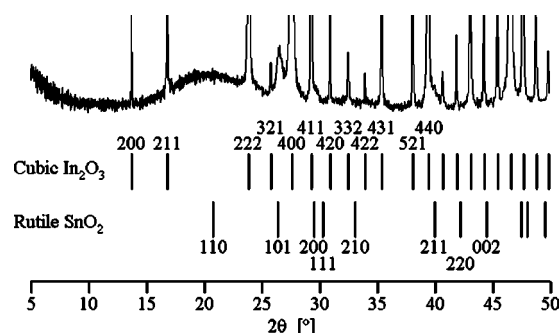


FIG. 8. High-resolution synchrotron powder pattern recorded from the ITO film covered with the FTO nanoparticles of 26 nm in average size. The peak positions from the PDF files are shown as vertical bars for cubic In_2O_3 and rutile-phase SnO_2 . X-ray wavelength: 0.1206237 nm, total scan time: 12 h.

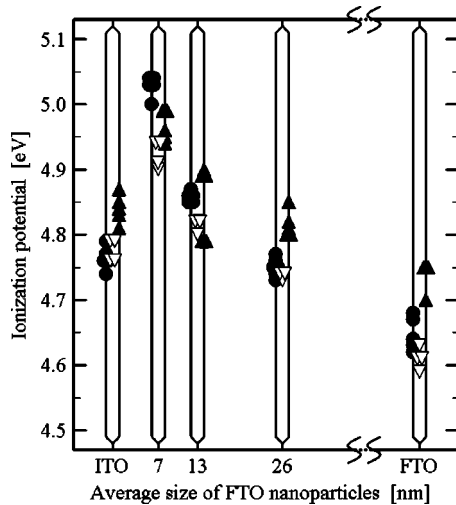


FIG. 9. Ionization potentials of the ITO films covered with FTO nanoparticles vs the average sizes of the FTO nanoparticles. Those for the ITO film and the FTO film are shown for comparison. Ionization potentials of the films were measured in three different states, as-grown (closed circle), after the 450 °C-60 min oxidizing treatment (inverted open triangle), and after the 600 °C-60 min reducing treatment (closed triangle). For clarity reasons, the closed symbols are horizontally shifted.

ticles has an ionization potential of 5.01 eV when the average FTO nanoparticle size is 7 nm, ~ 0.25 eV higher than the bare ITO surface. As the average size of the FTO nanoparticles increases, the ionization potential gradually decreases, eventually approaching the ionization potential of the FTO film (4.64 eV). It is inferred that these tendencies of the ionization potentials are not caused by the crystallinity of the FTO nanoparticles (Fig. 7). It is notable that the ionization potentials are marginally affected by the 450 °C-60 min oxidizing treatment or the 600 °C-60 min reducing treatment. The ionization potential of the ITO film covered with FTO nanoparticles is thermally stable. In Fig. 9, the mean ionization potentials of the as-grown ITO films covered with FTO nanoparticles of 7, 13, and 26 nm in size (D_{av}) are 5.01, 4.86, and 4.75 eV, respectively. The ionization potential may peak between $D_{av}=7$ nm and the bare ITO film without FTO nanoparticles whose ionization potential was measured to be 4.76 eV.

IV. DISCUSSION

It is surprising that the spray pyrolysis deposition using a simple perfume atomizer produces monodispersive FTO nanoparticles on the ITO surface. It is even more surprising that the FTO nanoparticles form single layers without growing on top.

The ability to control the ionization potentials simply by varying the spray cycle number would find a wide application in transparent conducting films. We give here a phenomenological account of the unique ionization potentials of the FTO nanoparticle-covered ITO films. An ITO film and a FTO film are degenerate semiconductors with high carrier densities over 10^{20} cm^{-3} . The Fermi levels of an ITO film of around 450 nm in thickness (E_F^{ITO}) and FTO nanoparticles (E_F^{FTO}) are located in each conduction band at room temperature when they are isolated from each other, as shown in Fig.

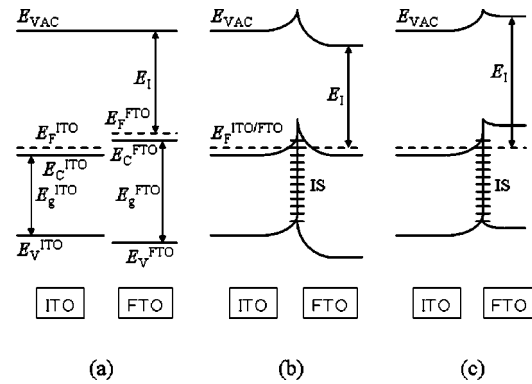


FIG. 10. Schematic band models of the interface between ITO film and FTO nanoparticle (a) before contact and (b), (c) after contact. FTO in (b) is assumed to be in the form of a thin film for explanation in the text. E_{VAC} : vacuum level, E_F : Fermi level, E_C : conduction-band bottom, and E_V : valence-band top. E_g shows the band gaps for ITO and FTO. The thick arrows, labeled with E_I , show the ionization potential for FTO.

10(a). In this scheme, the ionization potentials are defined by $E_{VAC}-E_F^{\text{ITO}}$ for ITO and $E_{VAC}-E_F^{\text{FTO}}$ for FTO, where E_{VAC} is the vacuum level. We have $E_C^{\text{ITO}}-E_V^{\text{ITO}}=E_g^{\text{ITO}}$ and $E_C^{\text{FTO}}-E_V^{\text{FTO}}=E_g^{\text{FTO}}$, where E_C , E_V , and E_g stand for the conduction-band bottom, the valence-band top, and the energy gap, respectively. The energy levels shown in Fig. 10(a) are estimated by taking the ionization potentials of the ITO film and the FTO film (4.76 and 4.64 eV) and the optical band-gap energies of the ITO film and the FTO film (3.6 and 3.8 eV) into account. When a FTO film comes in contact with an ITO film, a large number of interface states (IS) would be produced because of the lattice mismatch between ITO and FTO. These IS can trap and deplete electrons in the conduction bands of ITO and FTO, leading to a band bending near the interface [Fig. 10(b)]. This is the classical double Schottky-band model of an n - n isotype heterojunction with many IS.²⁷ If FTO in Fig. 10(b) is not a thin film but nanoparticles, as in our samples, electrons in the conduction band of a FTO nanoparticle can be completely depleted as the average size D_{av} of the FTO nanoparticle decreases because the number of electrons in the conduction band decreases in proportion to D_{av}^3 , while the number of IS decreases in proportion to D_{av}^2 . In completely depleted FTO nanoparticles, the Fermi level will come down below the bottom of the conduction band of a nanoparticle [Fig. 10(c)]. Here, band bending would not take place because the nanoparticle is too small in size to accommodate a band bending. In Fig. 10(c), the outermost-layer FTO nanoparticles would have an ionization potential E_I higher than those of FTO films and ITO films, depending on the condition. As the nanoparticles grow in size, the band bending is accommodated and E_I approaches the ionization potential of a thick FTO film. We have to be careful with the fact that while the ionization potentials presented in Fig. 9 refer to the mean potentials for the ITO surfaces deposited with FTO nanoparticles, they do not represent the ionization potentials of the nanoparticles themselves.

V. CONCLUSIONS

We produced ITO films uniformly covered with single layers of monodispersive FTO nanoparticles by intermittent

spray pyrolysis using conventional atomizers. These films were found to show a unique dependence of ionization potentials on the average size of the FTO nanoparticles. With a decrease in the average FTO size from 26 nm to 7 nm, the ionization potential increases from 4.75 eV to 5.01 eV. These are significantly higher than that for conventional ITO films (4.76 eV). A plausible account of the size-dependent ionization potential was given in conjunction with the energy states at the ITO/FTO interface and carrier depletion in the nanoparticles. Additional experiments are required to reach a more complete understanding of the size dependence. It is yet to be seen whether ITO films deposited with FTO particles of sizes less than 7 nm can reproducibly be grown and whether such surfaces have ionization potentials of 5.1–5.4 eV,^{4,5,28} which are desirable in organic electroluminescent and light-emitting applications.

ACKNOWLEDGMENTS

We wish to thank to Y. Nakajima, Riken Keiki Co. Ltd., for assistance in ionization potential measurements, and to N. Terada, Kagoshima University, for discussion about ionization potentials.

APPENDIX

The transmittance through an ITO film on a glass substrate, T_{sum} , is given by

$$T_{\text{sum}} = 1 - R_{\text{int}} - R_b, \quad (\text{A1})$$

where R_{int} and R_b are the reflectances from the film and the back surface of the glass substrate, respectively. Fresnel's law gives

$$R_b = \{(n_s - 1)/(n_s + 1)\}^2, \quad (\text{A2})$$

where n_s is the refractive index of the substrate glass. We put the refractive index of air at 1. The R_{int} at the minimal interference transmittance wavelength, λ_{min} , is given by

$$R_{\text{int}} = \{(n_{\text{ITO}}^2 - n_s)/(n_{\text{ITO}}^2 + n_s)\}^2, \quad (\text{A3})$$

where n_{ITO} is the refractive index of the ITO film ($n_{\text{ITO}} > n_s$). Combining Eqs. (A1) and (A3), we obtain

$$n_{\text{ITO}} = \left[\frac{2n_s}{1 - (1 - T_{\text{sum}} - R_b)^{1/2}} - n_s \right]^{1/2}. \quad (\text{A4})$$

n_s for the Corning 7059 glass used in our work is known to be 1.536 and 1.528 at 500- and 660-nm wavelengths, respectively. The thickness of the ITO film can be estimated from n_{ITO} , n_s , and λ_{min} if more than one minima are available in

the transmittance data. The optical absorptions of the ITO film and the glass substrate are negligible. For an ITO film on a glass substrate, optical theory shows

$$\lambda_{\text{min}} = 4n_{\text{ITO}}d_{\text{ITO}}/(2m + 1), \quad (\text{A5})$$

where d_{ITO} is the thickness of the ITO film and m is the interference order. Figure 4 shows transmittance minima at 500 and 660 nm, which correspond to $m=3$ and 2, respectively. Equation (A4) gives 1.94 and 1.87 for the n_{ITO} values at 500 and 660 nm, respectively.

- ¹T. Kawashima, H. Matsui, and N. Tanabe, *Thin Solid Films* **445**, 241 (2003).
- ²C. Goebbert, G. Gasparro, T. Schuler, T. Krajewski, and M. A. Aegerter, *J. Sol-Gel Sci. Technol.* **19**, 435 (2000).
- ³G. J. Fang, D. J. Li, and B. L. Yao, *J. Phys. D* **35**, 3096 (2002).
- ⁴J. S. Kim, M. Granström, R. H. Friend, N. Johansson, W. R. Salaneck, R. Daik, W. J. Feast, and F. Cacialli, *J. Appl. Phys.* **84**, 6859 (1998).
- ⁵S. F. J. Appleyard, S. R. Day, R. D. Pickford, and M. R. Willis, *J. Mater. Chem.* **10**, 169 (2000).
- ⁶F. Nüesch, E. W. Forsythe, Q. T. Le, Y. Gao, and L. J. Rothberg, *J. Appl. Phys.* **87**, 7973 (2000).
- ⁷K. Sugiyama, H. Ishii, Y. Ouchi, and K. Seki, *J. Appl. Phys.* **87**, 295 (2000).
- ⁸V. Christou, M. Etchells, O. Renault, P. J. Dobson, O. V. Salata, G. Beamson, and R. G. Egdel, *J. Appl. Phys.* **88**, 5180 (2000).
- ⁹Q. T. Le, F. Nüesch, L. J. Rothberg, E. W. Forsythe, and Y. Gao, *Appl. Phys. Lett.* **75**, 1357 (1999).
- ¹⁰L. Kronik *et al.*, *Appl. Phys. Lett.* **67**, 1405 (1995).
- ¹¹L. Kronik, M. Leibovitch, E. Fefer, V. Korobov, and Y. Shapira, *J. Electron. Mater.* **24**, 893 (1995).
- ¹²L. Kronik and Y. Shapira, *Surf. Sci. Rep.* **37**, 1 (1999).
- ¹³O. Lang, C. Pettenkofer, J. F. Sánchez-Royo, A. Segura, A. Klein, and W. Jaegermann, *J. Appl. Phys.* **86**, 5687 (1999).
- ¹⁴T. Fukano and T. Motohiro, *Sol. Energy Mater. Sol. Cells* **82**, 567 (2004).
- ¹⁵Y. Sawada, C. Kobayashi, S. Seki, and H. Funakubo, *Thin Solid Films* **409**, 46 (2002).
- ¹⁶S. Seki *et al.*, *J. Therm. Anal. Calorim.* **69**, 1021 (2002).
- ¹⁷*ASTM Designation: E 112-96* (American Society for Testing and Materials, Philadelphia, 1996).
- ¹⁸K. Kudo, *Optical Properties of Materials*, 2nd ed. (Ohmsha, Tokyo, 1990), pp. 169–180.
- ¹⁹M. Nagasawa and S. Shionoya, *Phys. Lett.* **22**, 409 (1966).
- ²⁰M. Nagasawa and S. Shionoya, *J. Phys. Soc. Jpn.* **30**, 158 (1971).
- ²¹J. Szuber and G. Czempik, *Vacuum* **48**, 289 (1997).
- ²²Joint Committee of Powder Diffraction Standard-International Center for Diffraction Data, Powder Diffraction File (Sec 53+) Card No. 06-0416 (2003).
- ²³Joint Committee of Powder Diffraction Standard-International Center for Diffraction Data, Powder Diffraction File (Sec 53+) Card No. 41-1445 (2003).
- ²⁴T. Ishida, H. Kobayashi, and Y. Nakato, *J. Appl. Phys.* **73**, 4344 (1993).
- ²⁵I. D. Parker, *J. Appl. Phys.* **75**, 1656 (1994).
- ²⁶M. Turrión, J. Bisquert, and P. Salvador, *J. Phys. Chem. B* **107**, 9397 (2003).
- ²⁷W. Heywang, *J. Mater. Sci.* **6**, 1214 (1971).
- ²⁸K. Z. Xing, M. Fahlman, X. W. Chen, O. Inganas, and W. R. Salaneck, *Synth. Met.* **89**, 161 (1997).